Influence of magnetic reconnection on the eruptive catastrophes of coronal magnetic flux ropes

Quanhao Zhang [1,2,3,*], **Xin Cheng** [4], **Rui Liu** [2,3,5], **Anchuan Song** [2,3,6], **Xiaolei Li** [2,3,6], **and Yuming Wang** [1,2,3]

[1] *Deep Space Exploration Laboratory/School of Earth and Space Sciences, University of Science and Technology of China, Hefei 230026, China*

[2] *CAS Key Laboratory of Geospace Environment, School of Earth and Space Sciences, University of Science and Technology of China, Hefei 230026, China*

[3] *CAS Center for Excellence in Comparative Planetology, University of Science and Technology of China, Hefei 230026, China*

[4] *School of Astronomy and Space Science, Nanjing University, Nanjing 210023, China*

[5] *Collaborative Innovation Center of Astronautical Science and Technology, Hefei, Anhui 230026, China*

[6] *Mengcheng National Geophysical Observatory, School of Earth and Space Sciences, University of Science and Technology of China, Hefei 230026, China*

Correspondence*:
Quanhao Zhang
zhangqh@ustc.edu.cn

ABSTRACT

Large-scale solar eruptive activities have a close relationship with coronal magnetic flux ropes. Previous numerical studies have found that the equilibrium of a coronal flux rope system could be disrupted if the axial magnetic flux of the rope exceeds a critical value, so that the catastrophe occurs, initiating the flux rope to erupt. Further studies discovered that the catastrophe does not necessarily exist: the flux rope system with certain photospheric flux distributions could be non-catastrophic. It is noteworthy that most previous numerical studies are under the ideal magnetohydrodynamic (MHD) condition, so that it is still elusive whether there is the catastrophe associated with the critical axial flux if magnetic reconnection is included in the flux rope system. In this paper, we carried out numerical simulations to investigate the evolutions of coronal magnetic rope systems under the ideal MHD and the resistive condition. Under the ideal MHD condition, our simulation results demonstrate that the flux rope systems with either too compact or too weak photospheric magnetic source regions are non-catastrophic versus varying axial flux of the rope, and thus no eruption could be initiated; if there is magnetic reconnection in the rope system, however, those flux rope systems could change to be capable of erupting via the catastrophe associated with increasing axial flux. Therefore, magnetic reconnection could significantly influence the catastrophic behaviors of flux rope system. It should be both the magnetic topology and the local physical parameters related to magnetic reconnection that determine whether the increasing axial flux is able to cause flux rope eruptions.

Keywords: Sun: filaments – Sun: prominences – Sun: flares – Sun: coronal mass ejections – Sun: magnetic fields – Sun: activity

1 INTRODUCTION

Large-scale solar eruptive activities are the principal cause of extreme space weather in Earth and planetary space environments (Švestka, 2001; Cheng et al., 2014; Lugaz et al., 2017; Gopalswamy et al., 2018). Different kinds of large-scale solar eruptions, including prominence/filament eruptions (Li et al., 2016a; Jenkins et al., 2018; Fan, 2020; Devi et al., 2021), flares (Chen et al., 2015; Li et al., 2016b; Cheung et al., 2019), and coronal mass ejections (CMEs, Shen et al., 2014; Lamy et al., 2019; Bemporad et al., 2022), are generally considered to be different manifestations of the eruptions of coronal magnetic flux rope (Zhang et al., 2001; Vršnak et al., 2005; Jiang et al., 2016; Chen et al., 2020; Liu, 2020). Therefore, investigating the initiation and evolution of flux rope eruptions is crucial not only for understanding solar eruptions, but also for space weather forecasting. Many theoretical models have been proposed to shed light on the physical scenario of coronal flux rope eruptions. These models are based on different kinds of physical mechanisms, such as ideal magnetohydrodynamic(MHD) instabilities (Török and Kliem, 2003; Aulanier et al., 2010; Guo et al., 2010; Savcheva et al., 2012; Keppens et al., 2019), magnetic reconnection (Antiochos et al., 1999; Chen and Shibata, 2000; Moore et al., 2001; Sterling and Moore, 2004; Archontis and Hood, 2008; Inoue et al., 2015), and the catastrophes of coronal flux ropes (Van Tend and Kuperus, 1978; Forbes and Priest, 1995; Lin and van Ballegooijen, 2002; Kliem et al., 2014; Zhang et al., 2021).

Many theoretical studies suggested that flux rope catastrophes are intriguing candidates for the source of solar eruptions (e.g., Lin and Forbes, 2000; Isenberg et al., 1993). In the flux rope catastrophe theory, the onset of the eruption is approached as the loss of equilibrium of the coronal flux rope system. Before the onset, the flux rope should be static or quasi-static (Török et al., 2013; Liu, 2020), indicating that the flux rope system is in equilibrium. If the equilibrium is not disrupted, the net force on the flux rope will always be zero, so that its state of motion will remains unchanged, i.e., no eruption of the flux rope could occur. Therefore, loss of equilibrium must occur during the onset of the eruption, and the resultant net force initiates the flux rope to erupt. This is the fundamental scenario of the catastrophe of coronal flux ropes. The investigation about when and how the catastrophe occurs is based on the equilibrium manifold (Forbes and Priest, 1995; Isenberg and Forbes, 2007; Kliem et al., 2014), which consists of all the equilibrium states of the flux rope system. For example, by analytically deriving the equilibrium manifold as a function of current within the flux rope, Van Tend and Kuperus (1978) for the first time discovered that there is a critical value of the current, beyond which there are no neighbouring equilibrium states so that the catastrophe occurs, which results in a discontinuous equilibrium manifold; this critical value is referred to as the catastrophic point. Many more analytical studies have verified that the catastrophe could occur in various types of coronal flux rope systems, resulting in the eruption of the flux rope (Priest and Forbes, 1990; Forbes and Priest, 1995; Lin and Forbes, 2000; Démoulin and Aulanier, 2010; Longcope and Forbes, 2014; Kliem et al., 2014). In addition, numerical simulations have also been carried out in many previous studies to investigate the catastrophes of coronal flux ropes (Forbes, 1990; Chen et al., 2007; Zhang et al., 2017a; Zhang et al., 2021). In numerical studies, the equilibrium manifold as a function of a certain physical parameter is obtained by simulating the equilibrium solutions of the flux rope system with different values of this parameter. For example, Su et al. (2011) discovered that the equilibrium manifold versus the axial magnetic flux of the flux rope is discontinuous at a critical value, beyond which a catastrophe occurs. Similar results are obtained in many other numerical studies (Bobra et al., 2008; Su et al., 2009, 2011; Zhang et al., 2017a,b), indicating that the axial flux of the rope should play an important role in initiating solar eruptions.

The catastrophe associated with the critical axial flux does not necessarily exist in coronal flux rope system. Previous numerical studies have demonstrated that the photospheric flux distributions of the background field greatly influence the catastrophic behaviors of coronal flux rope systems (Sun et al., 2007; Zhang et al., 2017a,b). Previous studies found that there are two types of non-catastrophic flux rope systems: if the photospheric flux is too concentrated toward the polarity inversion line (hereafter "compact" cases), or the total magnetic flux originating from the photospheric magnetic source regions is too weak (hereafter "weak" cases), the equilibrium manifold as a function of the rope's axial flux will be continuous so that no catastrophe could occur. It is still an open question why there is no catastrophe in these two types of flux rope system; Zhang et al. (2017b) inferred that the constraint from the background field on the flux rope might probably plays an considerable role. It is noteworthy that magnetic reconnection is completely prohibited in those studies, so that their conclusion about the two types of non-catastrophic flux rope systems is under the ideal MHD condition. Since the actual solar corona is resistive, there should be reconnection in actual coronal flux rope systems (Jiang et al., 2021; Yan et al., 2022; Bian et al., 2022). In fact, magnetic reconnection could not only change the magnetic topology, resulting in the redistribution of the Ampère's force (also known as Lorentz force in many papers), but the reconnection outflow could also push the flux rope upward (Chen et al., 2004; Wang et al., 2007; Xue et al., 2016; Cheng et al., 2020). This indicates that magnetic reconnection could contribute to the force balance of a coronal flux rope system, implying that the catastrophic behaviors of the rope system might differ under the ideal MHD and the resistive condition. Therefore, it is critical to assess the influence of magnetic reconnection on the catastrophic behaviors of coronal flux rope systems, so as to shed more light on the catastrophe theory for solar eruptions. To achieve this, we use a 2.5-dimensional MHD numerical model to simulate the catastrophic behaviors of the coronal flux rope systems with either compact or weak photospheric source regions. Both the equilibrium manifolds versus the axial magnetic flux under the ideal MHD and the resistive condition are simulated, based on which the influence of magnetic reconnection is investigated. The rest of this paper is arranged as follows: the numerical model and simulating procedures are introduced in Sect. 2, the simulation results are presented in Sect. 3, and the conclusion and discussion are given in Sect. 4.

2 NUMERICAL MODEL

2.1 Basic equations

The numerical model in our simulation is similar as those used in Zhang et al. (2017a,b). For 2.5-dimensional cases, by assuming all the quantities satisfy $\partial/\partial z = 0$, the magnetic field can be written in form of magnetic flux function ψ:

$$\mathbf{B} = \nabla\psi \times \hat{z} + B_z\hat{z}. \tag{1}$$

Here z is the unit vector in $z-$direction. Obviously, the divergence-free condition ($\nabla \cdot \mathbf{B} = 0$) is always satisfied. With the form given in Equation (1), the MHD equations in our simulations could be rewritten in the following form:

$$\frac{\partial \rho}{\partial t} + \nabla \cdot (\rho \boldsymbol{v}) = 0, \tag{2}$$

$$\frac{\partial \boldsymbol{v}}{\partial t} + \frac{2}{\rho \beta_0}(\triangle \psi \nabla \psi + B_z \nabla B_z + \nabla \psi \times \nabla B_z) + \boldsymbol{v} \cdot \nabla \boldsymbol{v}$$

$$+ \nabla T + \frac{T}{\rho} \nabla \rho + g \hat{\boldsymbol{y}} = 0, \tag{3}$$

$$\frac{\partial \psi}{\partial t} + \boldsymbol{v} \cdot \nabla \psi - \eta \triangle \psi = 0, \tag{4}$$

$$\frac{\partial B_z}{\partial t} + \nabla \cdot (B_z \boldsymbol{v}) + (\nabla \psi \times \nabla v_z) \cdot \hat{\boldsymbol{z}} - \eta \triangle B_z = 0, \tag{5}$$

$$\frac{\partial T}{\partial t} - \frac{\eta(\gamma - 1)}{\rho R}\left[(\triangle \psi)^2 + |\nabla \times (B_z \hat{\boldsymbol{z}})|^2\right]$$

$$+ \boldsymbol{v} \cdot \nabla T + (\gamma - 1)T \nabla \cdot \boldsymbol{v} = 0, \tag{6}$$

where

$$\triangle \psi = \frac{\partial^2 \psi}{\partial x^2} + \frac{\partial^2 \psi}{\partial y^2}, \quad \triangle B_z = \frac{\partial^2 B_z}{\partial x^2} + \frac{\partial^2 B_z}{\partial y^2}. \tag{7}$$

Here ρ is the density, $\boldsymbol{v}$ the velocity, T the temperature, $\gamma = 5/3$ the polytropic index, g the gravity, η the resistivity, and $\beta_0 = 0.1$ the characteristic ratio of the gas pressure to the magnetic pressure, which is comparable to the value in quiescent regions (Anzer and Heinzel, 2007; Hillier et al., 2012; Xia et al., 2012). The x, y, and z−component of the quantities are denoted by the subscript x, y, z. The radiation and the heat conduction in the energy equation are neglected. The numerical domain in our simulation is $0 < x < 200$ Mm, $0 < y < 500$ Mm; it is discretized into 200×250 uniform meshes.
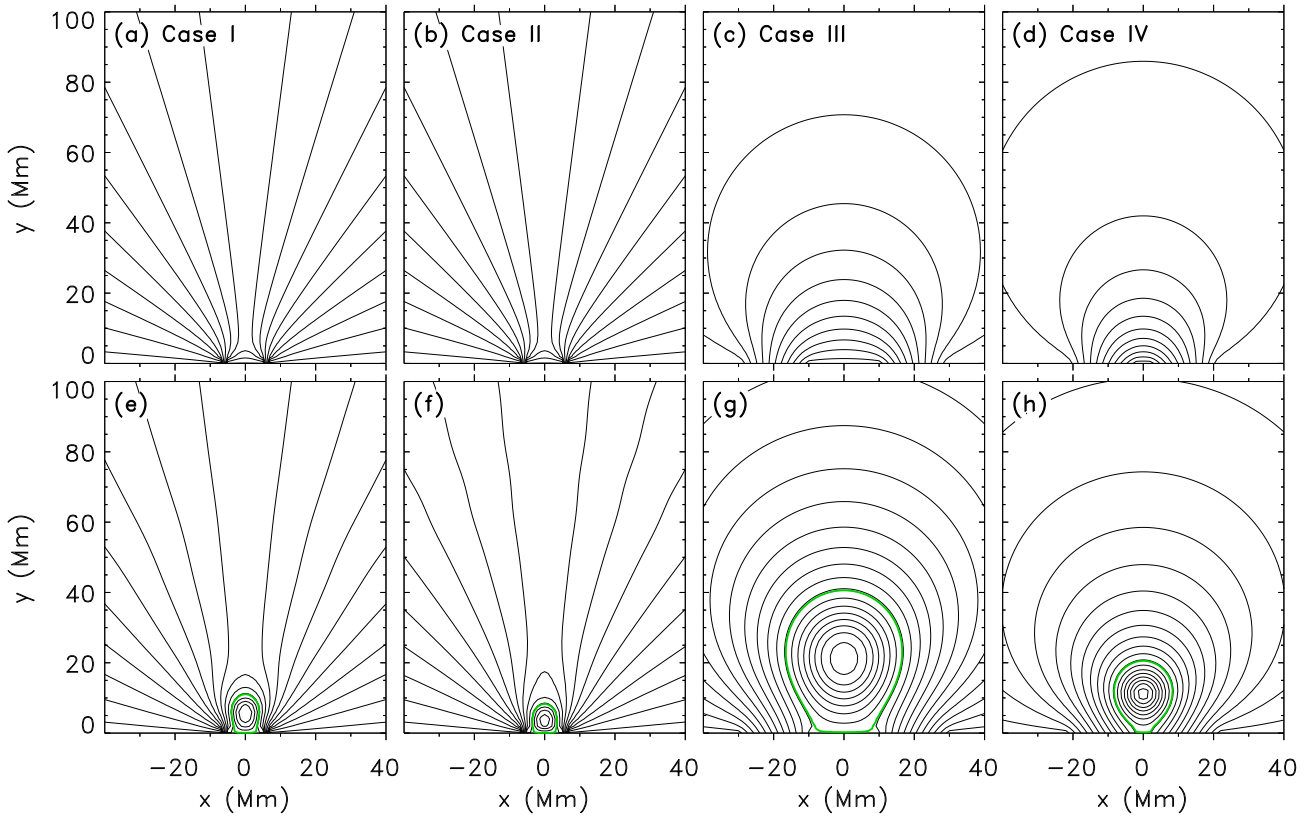
2.2 Initial state

The initial states in our simulations are constructed by numerical procedures. Here we first use the complex variable method (e.g., Hu and Liu, 2000; Zhang et al., 2017a) to construct the background field originating from photospheric magnetic source regions. The background field is a partially open bipolar field, with a negative surface magnetic charge located at the lower boundary within $-b < x < -a$, and a positive one within $a < x < b$; the distance between the two source regions is $D = 2a$, and the width of the source region $W = b - a$. The background field in $x - y$ plane could then be expressed in the complex variable form as:

$$f(\omega) \equiv B_x - iB_y = \lambda \frac{(\omega + iy_N)^{1/2}(\omega - iy_N)^{1/2}}{F(a, b, y_N)} \ln\left(\frac{\omega^2 - a^2}{\omega^2 - b^2}\right), \tag{8}$$

where $\omega = x + iy$,

$$F(a, b, y_N) = \frac{1}{b - a} \int_a^b (x^2 + y_N^2)^{1/2} dx = \frac{1}{2(b - a)} \times$$

$$\left[b(b^2 + y_N^2)^{1/2} - a(a^2 + y_N^2)^{1/2} + y_N^2 \ln\left(\frac{b + (b^2 + y_N^2)^{1/2}}{a + (a^2 + y_N^2)^{1/2}}\right)\right], \tag{9}$$

Figure 1. The magnetic configurations of the background fields and initial states in the simulation. Panel (a) is the background field for Case I, and panel (e) is the corresponding initial state; panels (b) and (f), (c) and (g), (d) and (h) are those for Case II, III, IV, respectively. The black curves are the magnetic field lines, and the green curves mark the boundary of the flux rope. The physical parameters for the background fields and initial states are tabulated in Table 1.

and the neutral point of the background field is at $(y = y_N, x = 0)$. As indicated by Equation (8), the magnetic field strength of the background field is proportional to the dimensionless parameter λ. The magnetic flux function within the domain could then be calculated by:

$$\psi(x, y) = \text{Im}\left\{\int f(\omega)d\omega\right\}, \tag{10}$$

With calculated the flux function ψ, and by letting $B_z = 0$ in the background field, the magnetic configuration of the background field is obtained (Equation (1)). In particular, the flux function of the background field at the lower base, ψ_i, could be calculated as:

$$\psi_i = \psi(x, 0) = \begin{cases} \lambda\widehat{\psi_0}\pi(b - a), & |x| < a \\ \lambda\widehat{\psi_0}\pi(b - a)F(|x|, b, y_N)/F(a, b, y_N), & a \leqslant |x| \leqslant b \\ 0, & |x| > b \end{cases} \tag{11}$$

and the flux function at the neutral point of the background field is

$$\psi_N = \psi(0, y_N) = \frac{\lambda\widehat{\psi_0}\pi(b^2 - a^2)}{2F(a, b, y_N)} \tag{12}$$

Here $\psi_c = \lambda\pi(b-a)\widehat{\psi_0}$ ($\widehat{\psi_0} = 37.25$ Mx cm^{-2}) is the total magnetic flux emanating upward from the positive photospheric source region per unit length along $z-$direction, i.e. ψ_c represents the intensity of background magnetic field originating from the photospheric source regions. The ratio of the background field's open magnetic flux to its total magnetic flux could then be calculated by:

$$\kappa = \frac{\psi_N}{\psi_c}. \tag{13}$$

For a given background magnetic field, its characteristic physical parameters include D, W, ψ_c and κ, which could be calculated with a group of given a, b, y_N, and λ. For example, by letting $a = 5.00$ Mm, $b = 7.00$ Mm, $y_N = 4.49$ Mm, $\lambda = 1.0$, the calculated background configuration is plotted in Fig. 1(a), and the characteristic parameters of this background field are: $D = 10$ Mm, $W = 2$ Mm, $\psi_c = 2.34 \times 10^{10}$ Mx cm^{-1}, and $\kappa = 0.80$, as tabulated in the second column (Case I) in Table 1. The initial corona in our simulations is static and isothermal:

$$T_c \equiv T(0, x, y) = 1 \times 10^6 \text{ K}, \quad \rho_c \equiv \rho(0, x, y) = \rho_0 e^{-gy}, \tag{14}$$

where $\rho_0 = 3.34 \times 10^{-13}$ kg m^{-3}.

With the background field obtained above, we let a flux rope emerge from the lower base of the domain with similar simulating procedures as those introduced in, e.g., Zhang et al. (2017a) and Zhang et al. (2020), and then relax the flux rope system to equilibrium. The resultant equilibrium state consisting of a flux rope embedded in the background field is the constructed initial state. For the background field plotted in Fig. 1(a), the constructed initial state is illustrated in Fig. 1(e). The magnetic properties of a flux rope could be characterized by its magnetic fluxes, including the total axial flux passing through the rope's cross section, $\Phi_z = \iint B_z dS$, and the annular flux per unit length along z-direction of the rope, Φ_p; in 2.5 dimensional cases, the poloidal flux is calculated as:

$$\Phi_p = \psi_{rc} - \psi_{rb}, \tag{15}$$

where ψ_{rc} and ψ_{rb} are the flux function ψ at the center and the boundary of the flux rope, respectively. For the initial state illustrated in Fig. 1(e), $\Phi_{z0} = 1.416 \times 10^{19}$ Mx and $\Phi_{p0} = 7.450 \times 10^9$ Mx cm^{-1}. With this initial state, we could further simulate the catastrophic behaviors of the coronal flux rope system with the given photospheric magnetic conditions (detailed simulating procedures are introduced in Sect. 2.3). It is noteworthy that the radius of the flux rope in our simulation is finite, so that the thin-rope approximation is not satisfied. Under this circumstance, the initial state could only be obtained by numerical procedures.

In our simulations, apart from those plotted in Fig. 1(a) and Fig. 1(e), we also construct another three groups of background field and initial state with similar procedures introduced above, and their parameters are tabulated in Table 1; all these 4 cases are marked as Case I~IV, respectively. The background field and the initial state in Case II are illustrated in Fig. 1(b) and Fig. 1(f), respectively. As shown by the the second and the third column in Table 1, D, W, and κ in Case I and Case II are the same; the only difference in the characteristic parameters of the background field between these two cases is that ψ_c in Case II is much smaller than that in Case I (achieved by adjusting λ to 0.1 in Case II), i.e. the intensity of the background magnetic field originating from the photospheric source regions in Case II is much weaker than those in Case I. For Case III and Case IV, the corresponding background fields and initial states are illustrated in Fig. 1(c)-1(d) and Fig. 1(g)-1(h), respectively. As shown in the last two columns

Table 1. The parameters of the background fields and the initial states for Case I-IV.

	Case I	Case II	Case III	Case IV
a (Mm)	5.00	5.00	10.00	2.00
b (Mm)	7.00	7.00	30.00	22.00
y_n (Mm)	4.49	4.49	1999.89	1199.93
λ	1.00	0.10	0.10	0.10
D (Mm)	10.00	10.00	20.00	4.00
W (Mm)	2.00	2.00	20.00	20.00
ψ_c (Mx cm^{-1})	2.340×10^{10}	0.234×10^{10}	2.340×10^{10}	2.340×10^{10}
κ	0.80	0.80	0.01	0.01
Φ_{z0} (Mx)	1.416×10^{19}	1.118×10^{18}	5.960×10^{19}	2.421×10^{19}
Φ_{p0} (Mx cm^{-1})	7.450×10^9	7.450×10^8	1.490×10^{10}	1.490×10^{10}

* Here a, b, y_n, and λ are the parameters used to construct the background field; D, W, ψ_c, and κ are the corresponding characteristic physical parameters of the background field; Φ_{z0} and Φ_{p0} are the magnetic fluxes of the initial flux rope.

in Table 1, the characteristic parameters of the background field in these two cases are the same, except that the distance between the source regions, D, is much smaller in Case IV than that in Case III.

2.3 Simulating procedures

Starting from each of the four initial states obtained above, we simulate the equilibrium states of the corresponding flux rope system with different axial magnetic fluxes of the rope: from $0 \sim 20\tau_A$ ($\tau_A = 17.4$ s is the typical Alfvén transit time), the axial flux Φ_z and the poloidal flux Φ_p are adjusted from the initial values to a certain group of target values (Φ_z^1, Φ_p^t), and from $20 \sim 300\tau_A$, the magnetic system is relaxed to equilibrium, with the magnetic fluxes fixed at the target values (Φ_z^1, Φ_p^t). We note that the conservation of the poloidal flux is achieved by fixing the flux function at the rope center, ψ_{rc}, during the relaxation (Equation (15)). The final state at $t = 300\tau_A$ is regarded as the equilibrium state of the flux rope system for Φ_z^1. During the relaxation, magnetic reconnection is either included or completely prohibited during the relaxation, corresponding to the resistive condition and ideal MHD condition, respectively. For the simulations under the resistive condition, anomalous resistivity is used:

$$\eta = \begin{cases} 0, & j \le j_c \\ \eta_m \mu_0 v_0 L_0 (\frac{j}{j_c} - 1)^2. & j > j_c \end{cases} \tag{16}$$

Here η_m=0.10, $L_0 = 10^7$ m, $v_0 = 128.57$ km s^{-1}, $j_c = 2.96 \times 10^{-5}$ A m^{-2}, and μ_0 is the vacuum magnetic permeability. On the other hand, for the simulations under the ideal MHD conditions, we use similar simulating procedures as those in Zhang et al. (2017a,b) during the relaxation to prohibit the reconnection: first set the resistivity η to be 0, and then reassign the flux function ψ along the current sheet with the initial values at each time step, so as to keep ψ invariant along the current sheet. Since any reconnection will reduce the value of ψ at the current sheet, both physical and numerical reconnections are prohibited with the simulating procedures introduced above. For the given target values Φ_z^1, we are able to simulate

two equilibrium states with the simulating procedures above: if reconnection is prohibited during the relaxation, the resultant equilibrium state is under ideal MHD condition, whereas the resultant equilibrium state is under resistive condition if reconnection is included during the relaxation.

Similar simulations are repeated for different target values $((\Phi_z^2, \Phi_p^t), (\Phi_z^3, \Phi_p^t), ...)$ so as to obtain equilibrium states with different Φ_z. Eventually, all the calculated equilibrium states without reconnection constitute a equilibrium manifold under the ideal MHD condition, and all those with reconnection constitute the equilibrium manifold under the resistive condition.

In our simulations, the quantities at the lower boundary of the domain are fixed, so that the lower boundary corresponds to the photosphere. Symmetric boundary condition is used at the left side of the domain ($x = 0$). At the other boundaries, increment equivalent extrapolation (Zhang et al., 2017a,b) is used to prescribe the boundary quantities:

$$U_b^{n+1} = U_{b-1}^{n+1} + U_b^n - U_{b-1}^n, \tag{17}$$

where U represents the quantities. The superscript n denote the quantities at the current time step, and $n + 1$ the next time step; the subscript b indicates the quantities at the boundary, and $b - 1$ those at the grids next to the boundary.
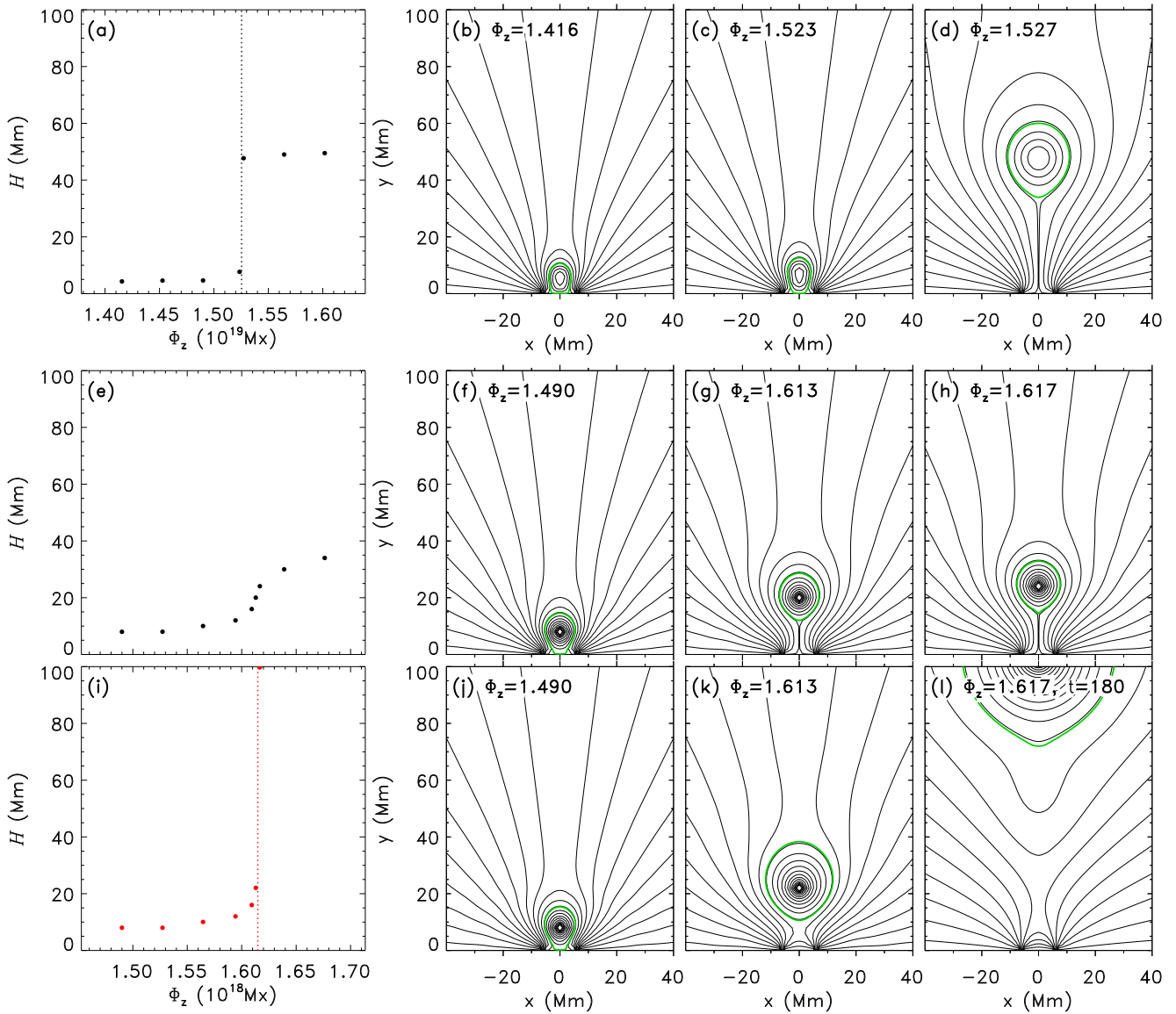
3 SIMULATION RESULTS

3.1 Weak cases

The equilibrium manifold as a function of the axial flux Φ_z under the ideal MHD condition for Case I is plotted in Fig. 2(a). All the equilibrium states have the same $\Phi_p = 7.45 \times 10^9$ Mx cm^{-1}. Obviously, this equilibrium manifold is discontinuous: the flux rope keeps sticking to the photosphere (Fig. 2(b)-2(c)) before reaching a critical axial flux at about 1.527×10^{18} Mx, which is marked by the black vertical dotted line in Fig. 2(a); otherwise, the flux rope jumps upward (Fig. 2(d)), indicating that a catastrophe occurs. Therefore, the flux rope system in Case I is catastrophic under the ideal MHD condition.

The equilibrium manifold under the ideal MHD condition for Case II is plotted in Fig. 2(e), and all the equilibrium states have the same $\Phi_p = 2.980 \times 10^9$ Mx cm^{-1}. Different from that in Fig. 2(a), the equilibrium manifold under the ideal MHD condition for Case II is continuous: the height of the rope axis, H, gradually rises as Φ_z increases, and the magnetic configurations of some equilibrium states are illustrated in Fig. 2(f)-2(h). The evolution of the flux rope system during the relaxation to simulate the equilibrium state in Fig. 2(g) is shown in Fig. 3(a1)-3(a4). After Φ_z is increased to 1.613×10^{18} Mx at $t = 20\tau_A$ (Fig. 3(a1)), the flux rope gradually rises and then is suspended in the corona (Fig. 3(a2)-3(a3)), until it reaches equilibrium (Fig. 3(a4), the same as Fig. 2(g)). Although a current sheet is formed by the magnetic field of opposite directions below the rope, the magnetic reconnection is prohibited by the simulating procedures introduced in Sect. 2.3. These simulation results demonstrate that the flux rope system in Case II is non-catastrophic so that no eruption could be initiated under the ideal MHD condition. As introduced in Sect. 2.2, the only difference in the characteristic parameters of the background field in Case I and Case II is ψ_c: the intensity of the background magnetic field originating from the photospheric source regions in Case II is much weaker than those in Case I, i.e. Case II is a "weak" case. This result is consistent with the conclusions in Zhang et al. (2017a,b).

To investigate the influence of magnetic reconnection on the catastrophic behaviors of flux rope systems with weak photospheric source regions, we also simulate the equilibrium manifold under the resistive
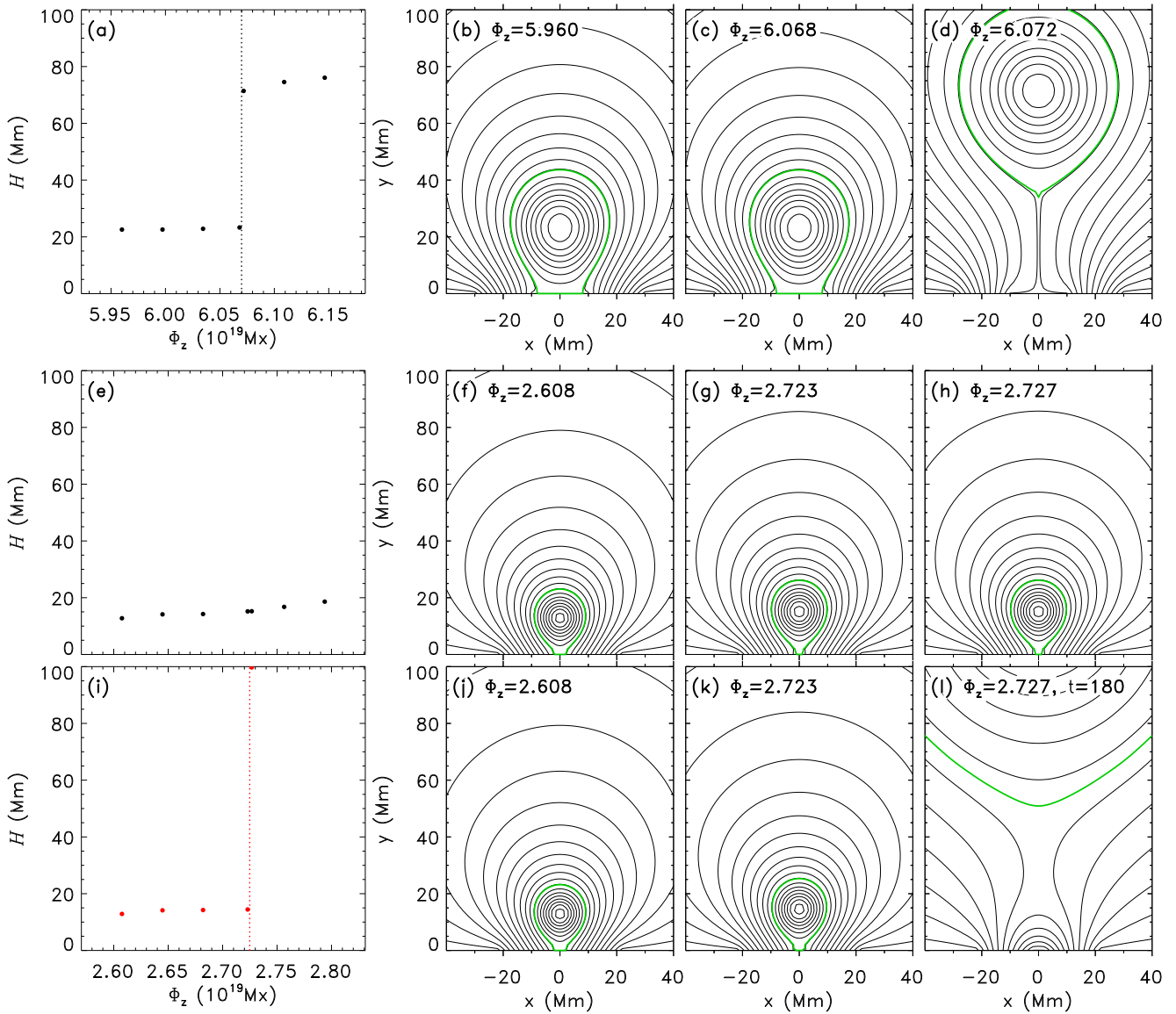
Figure 2. The simulation results for Case I and Case II. Panel (a) is the equilibrium manifold for Case I under the ideal MHD condition; panels (b)-(d) are the magnetic configuration of the simulated equilibrium states for Case I, and the corresponding Φ_z is marked at the top of each panel. Panels (e)-(h) and panels (i)-(l) are the simulation results for Case II under the ideal MHD and the resistive condition, respectively; the red vertical dotted line in panel (i) denote the catastrophic point Φ_{zc}^w. The green curves mark the boundary of the flux rope.

condition for Case II, as plotted in Fig. 2(i). Obviously, if there is magnetic reconnection in the flux rope system, the equilibrium manifold is discontinuous: there is a critical axial magnetic flux $\Phi_{zc}^w \approx 1.617 \times 10^{18}$ Mx, which is marked by the red vertical dotted line in Fig. 2(i). As shown in Fig. 2(i), H gradually rises as Φ_z increases before reaching Φ_{zc}^w. Fig. 2(k) illustrate the magnetic configuration of the equilibrium state with $\Phi_z = 1.613 \times 10^{18}$ Mx, i.e., the equilibrium state right before Φ_{zc}^w is reached, and the evolution of the flux rope system to reach this equilibrium state is shown in Fig. 3(b1)-3(b4). Comparing with the simulation results without reconnection in Fig. 3(a1)-3(a4), it is demonstrated that magnetic reconnection occurs in the current sheet below the flux rope (Fig. 3(b2)-3(b3)), resulting in closed arcades below the rope. The flux rope does not further rises but remains suspended, and eventually evolves to equilibrium
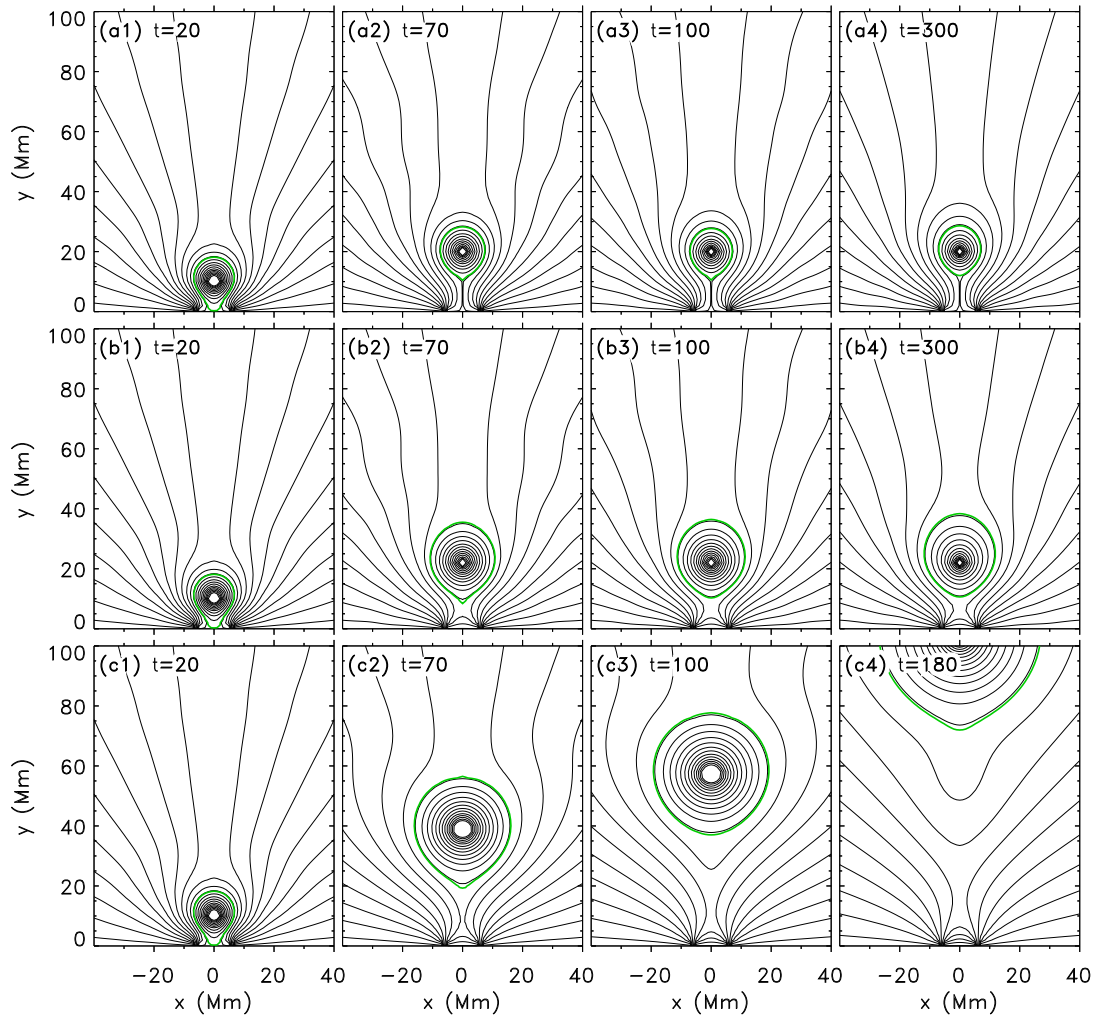
Figure 3. The temporal evolutions of the flux rope for Case II. Panels (a1)-(a4) illustrate the evolution of the flux rope during the relaxation to simulate the equilibrium state in Fig. 2(g). Panels (b1)-(b4) illustrate the evolution of the flux rope during the relaxation to simulate the equilibrium state in Fig. 2(k), which is the equilibrium state right before $\Phi_z = \Phi_{zc}^w$ is reached under the resistive condition; Panels (b1)-(b4) illustrate the evolution right after $\Phi_z = \Phi_{zc}^w$ is reached under the resistive condition.

(Fig. 3(b4), the same as Fig. 2(g)). As introduced in Sect. 2.2, $B_z = 0$ in the background field, so that the reconnection has no effect on the total axial magnetic flux of the rope. If Φ_z increases to reach Φ_{zc}^w, the flux rope is initiated to erupt, as shown by the evolution of the flux rope system illustrated in Fig. 3(c1)-3(c4): the flux rope does not remains suspended in the corona, but keeps rising after Φ_z is increased to Φ_{zc}^w, resulting in the eruption of the flux rope. Obviously, the evolutions of the flux rope system before and after Φ_z reaches Φ_{zc}^w are quite different if magnetic reconnection is included, indicating that there is a catastrophe in the flux rope system, and Φ_{zc}^w is the catastrophic point. We note that there is no equilibrium state if the catastrophe occurs under the ressitive condition, so that we illustrate the state at $t = 180\tau_A$ in Fig. 2(l) (the same as Fig. 3(c4)) as the characteristic state for $\Phi_z = \Phi_{zc}^w$, and the corresponding red point in Fig. 2(i) is plotted at the top boundary. Our simulation results suggest that the magnetic flux rope system with weak photospheric source regions could also be catastrophic if magnetic reconnection is included in the system.

Figure 4. The simulation results for Case III and Case IV. Panel (a)-(d) are the simulation results for Case III under the ideal MHD condition. Panels (e)-(h) and panels (i)-(l) are the simulation results for Case IV under the ideal MHD condition and the resistive condition, respectively; the red vertical dotted line in panel (i) denote the catastrophic point Φ_{zc}^c. The green curves mark the boundary of the flux rope.

3.2 Compact cases

The simulation results under the ideal MHD condition for Case III and Case IV are illustrated in Fig. 4(a)-4(d) and Fig. 4(e)-4(h), respectively, in which all the simulated equilibrium states have the same $\Phi_p = 1.490 \times 10^{10}$ Mx cm^{-1}. As introduced in Sect. 2.2 and Table 1, the distance between the photospheric source regions is much smaller in Case IV than that in Case III. As shown in Fig. 4(a), the flux rope system in Case III is catastrophic: the catastrophe occurs if Φ_z reaches 6.072×10^{19} Mx, as marked by the black vertical dotted line in Fig. 4(a). The flux rope system in Case IV, however, is non-catastrophic; its equilibrium manifold is continuous. This indicates Case IV is a "compact" case, which is also consistent with Zhang et al. (2017a,b). The evolution of the flux rope system to reach the equilibrium state in Fig. 4(g) is shown in Fig. 5(a1)-5(a4).
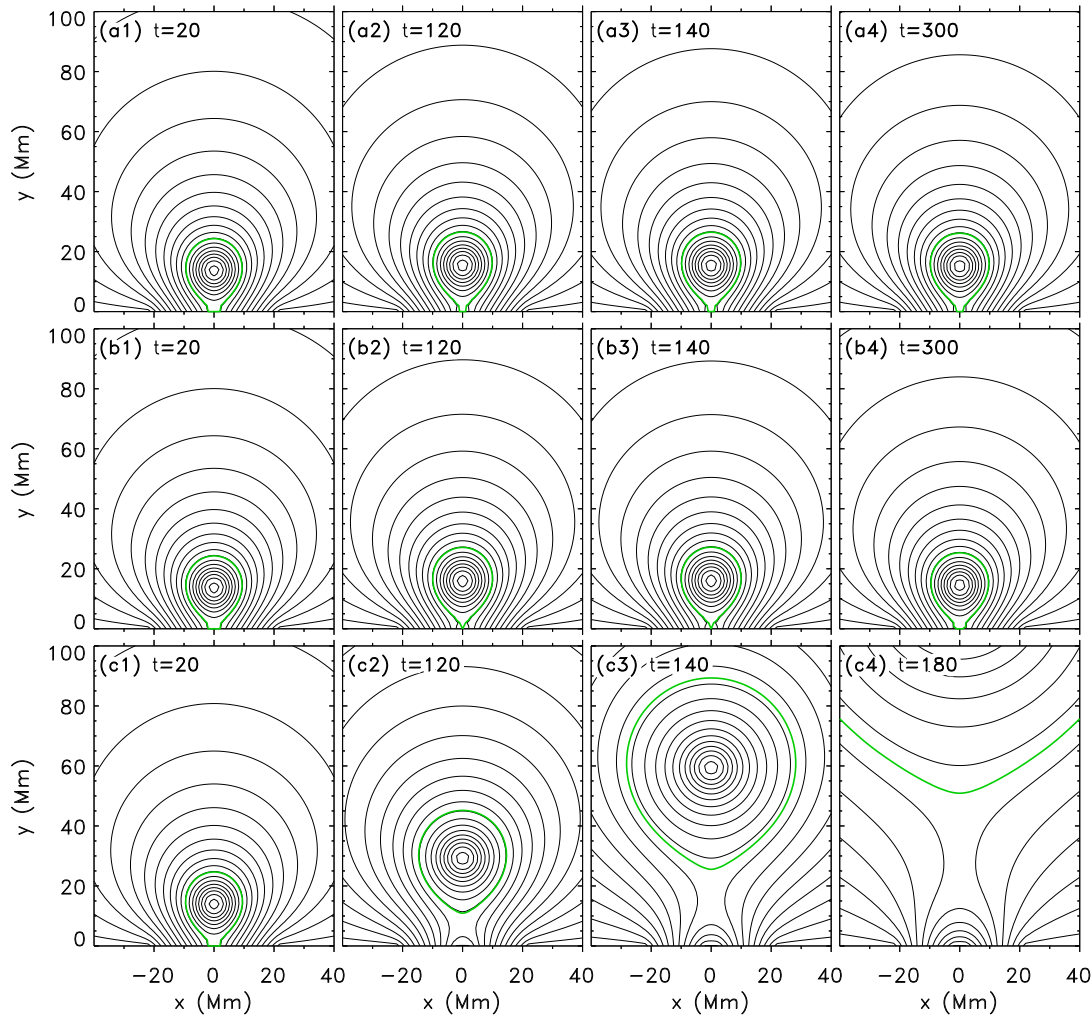
Figure 5. The temporal evolution of the flux rope for Case IV. Panels (a1)-(a4) illustrate the evolution of the flux rope during the relaxation to simulate the equilibrium state in Fig. 4(g). Panels (b1)-(b4) illustrate the evolution of the flux rope during the relaxation to simulate the equilibrium state in Fig. 4(k), which is the equilibrium state right before $\Phi_z = \Phi_{zc}^c$ is reached under the resistive condition; Panels (b1)-(b4) illustrate the evolution right after $\Phi_z = \Phi_{zc}^c$ is reached under the resistive condition.

Similar as those in Sect. 3.1, we also simulate the equilibrium manifold under the ressitive condition for Case IV, so as to investigate the influence of magnetic reconnection on the catastrophic behaviors of flux rope systems with compact photospheric source regions. As plotted in Fig. 4(i), there is a critical axial magnetic flux $\Phi_{zc}^c \approx 2.727 \times 10^{19}$ Mx if magnetic reconnection is included in the simulation, as marked by the red vertical dotted lines in Fig. 4(i). The evolutions of the flux rope system before and after Φ_z reaches Φ_{zc}^c are quite different: if Φ_z is smaller than Φ_{zc}^c, the flux rope does not erupt but evolves to equilibrium (Fig. 5(b1)-5(b4)); if Φ_{zc}^c is reached, the flux rope erupts(Fig. 5(c1)-5(c4)). This indicates that a catastrophe associated with the increasing axial magnetic flux of the rope could occur under the ressitive condition. For comparison, the topologies of the equilibrium states before and after Φ_z reaches Φ_{zc}^c are quite similar if there is no reconnection (Fig. 4(g) and Fig. 4(h)). This further confirms that it is the magnetic reconnection that changes the catastrophic behaviors of the flux rope system versus varying axial flux. Therefore, the flux rope system with compact photospheric source regions could also be catastrophic if there is magnetic reconnection in the rope system.

4 DISCUSSION AND CONCLUSION

In this paper, we investigate the influence of magnetic reconnection on the catastrophic behaviors of coronal flux rope systems associated with increasing axial magnetic flux of the rope. Under the ideal MHD condition, our simulation results demonstrate that coronal flux rope systems with either too compact or too weak photospheric source regions are non-catastrophic versus varying axial magnetic flux. Under the resistive condition, however, both the flux rope system with too compact and too weak photospheric source regions could change to be catastrophic: the catastrophe occurs when the axial flux of the rope increases to reach the critical value, so that the eruption of the flux rope is initiated.

Our simulation results demonstrate that the equilibrium manifolds of a coronal flux rope system could be quite different under the ideal MHD and the resistive condition (e.g., Fig. 2(e) and Fig. 2(i)). This indicates that magnetic reconnection should play a considerable role in determining the force balance and the corresponding the loss of equilibrium associated with increasing axial magnetic flux in coronal flux rope systems. We note that the continuous equilibrium manifold (Fig. 2(e)) is different from the discontinuous equilibrium manifold (Fig. 2(i)) in essence. It is widely accepted that solar eruptions should be caused by photospheric and coronal disturbances (Lin et al., 2003), the spatial range of which, however, is much smaller than that of solar eruptions (Priest, 2014). If the equilibrium manifold of a flux rope system is continuous, the variations of Φ_z caused by photospheric or coronal disturbances could only cause flux rope movements on a spatial scale comparable to the disturbance itself. In contrast, if the equilibrium manifold is discontinuous, there is a critical axial flux of Φ_z, so that even an infinitesimal increment of Φ_z to reach this critical value could cause the catastrophe of the flux rope, resulting in much larger scale of movement of the flux rope than that of the disturbances. Therefore, solar eruptions could only be initiated in the coronal flux rope system whose equilibrium manifold is discontinuous.

In previous studies, the forecasting of solar eruptions is generally based on the photospheric magnetic flux distributions within solar active regions (e.g., Leka and Barnes, 2007; Bobra and Couvidat, 2015; Toriumi and Wang, 2019; Korsós et al., 2020). However, as revealed by our simulation results, not only do different photospheric flux distributions result in different evolutions of the flux rope system, but the catastrophic behaviors of a particular flux rope system with given photospheric flux distribution could also differ under the ideal MHD condition and the resistive condition. This implies that two active regions with similar photospheric flux distribution might be quite different in their ability to initiate solar eruptions, provided that the local resistivity and characteristic spatial scale differs in the two active regions. Therefore, it should not be sufficient to predict whether a solar active region will be a potential source region for solar eruptions based solely on its photospheric magnetic flux distributions. Our simulation results suggest that both the magnetic topology and the local physical parameters related to magnetic reconnection determine whether increasing axial flux is able to cause flux rope eruptions.

There are also catastrophes associated with other physical parameters of flux rope systems, such as increasing shear of the background field (Chen et al., 2006) and decreasing mass of the rope (Jenkins et al., 2019; Zhang et al., 2021). It could be inferred that the catastrophic behaviors associated with those parameters might probably also be determined by both the magnetic topology and whether the magnetic system is resistive. In our future work, we will carry out more simulations to further investigate the influence of magnetic reconnection on different kinds catastrophes.

CONFLICT OF INTEREST STATEMENT

The authors declare that the research was conducted in the absence of any commercial or financial relationships that could be construed as a potential conflict of interest.

AUTHOR CONTRIBUTIONS

Quanhao Zhang carried out the numerical simulation, analyzed the simulation results, and prepared the manuscript. Xin Cheng contributed to the initial inspiration of this study, and the improvement of the numerical model. Rui Liu contributed to the analysis of the simulation results. Anchuan Song, Xiaolei Li, and Yuming Wang joined in the discussions about the simulation results.

FUNDING

ACKNOWLEDGMENTS

DATA AVAILABILITY STATEMENT

The simulation results in this study are included in the article; if there is any further inquiry, please contact the corresponding author.

REFERENCES

Antiochos, S. K., DeVore, C. R., and Klimchuk, J. A. (1999). A model for solar coronal mass ejections. *Astrophysical Journal*. 510, 485–493. doi:10.1086/306563

Anzer, U. and Heinzel, P. (2007). Is the magnetic field in quiescent prominences force-free? *Astronomy and Astrophysics*. 467, 1285–1288. doi:10.1051/0004-6361:20066817

Archontis, V. and Hood, A. W. (2008). A Flux Emergence Model for Solar Eruptions. *Astrophysical Journal Letters*. 674, L113. doi:10.1086/529377

Aulanier, G., Török, T., Démoulin, P., and DeLuca, E. E. (2010). Formation of torus-unstable flux ropes and electric currents in erupting sigmoids. *Astrophysical Journal*. 708, 314–333. doi:10.1088/0004-637X/708/1/314

Bemporad, A., Andretta, V., Susino, R., Mancuso, S., Spadaro, D., Mierla, M., et al. (2022). Coronal mass ejection followed by a prominence eruption and a plasma blob as observed by solar orbiter. *Astronomy and Astrophysics*. 665, A7. doi:10.1051/0004-6361/202243162

Bian, X., Jiang, C., and Feng, X. (2022). The role of photospheric converging motion in initiation of solar eruptions. *Frontiers in Astronomy and Space Sciences* 9, 982108. doi:10.3389/fspas.2022.982108

Bobra, M. G. and Couvidat, S. (2015). Solar flare prediction using sdo/hmi vector magnetic field data with a machine-learning algorithm. *Astrophysical Journal.* 798, 135. doi:10.1088/0004-637X/798/2/135

Bobra, M. G., van Ballegooijen, A. A., and DeLuca, E. E. (2008). Modeling Nonpotential Magnetic Fields in Solar Active Regions. *Astrophysical Journal.* 672, 1209–1220. doi:10.1086/523927

Chen, B., Yu, S., Reeves, K. K., and Gary, D. E. (2020). Microwave spectral imaging of an erupting magnetic flux rope: Implications for the standard solar flare model in three dimensions. *Astrophysical Journal Letters.* 895, L50. doi:10.3847/2041-8213/ab901a

Chen, H., Zhang, J., Ma, S., Yang, S., Li, L., Huang, X., et al. (2015). Confined flares in solar active region 12192 from 2014 october 18 to 29. *Astrophysical Journal Letters.* 808, L24. doi:10.1088/2041-8205/808/1/L24

Chen, P. F. and Shibata, K. (2000). An emerging flux trigger mechanism for coronal mass ejections. *Astrophysical Journal.* 545, 524–531. doi:10.1086/317803

Chen, P. F., Shibata, K., Brooks, D. H., and Isobe, H. (2004). A reexamination of the evidence for reconnection inflow. *Astrophysical Journal Letters.* 602, L61–L64. doi:10.1086/382479

Chen, Y., Chen, X. H., and Hu, Y. Q. (2006). Catastrophe of coronal flux rope in unsheared and sheared bipolar magnetic fields. *Astrophysical Journal.* 644, 587–591. doi:10.1086/503540

Chen, Y., Hu, Y. Q., and Sun, S. J. (2007). Catastrophic eruption of magnetic flux rope in the corona and solar wind with and without magnetic reconnection. *Astrophysical Journal.* 665, 1421–1427. doi:10.1086/519551

Cheng, X., Ding, M. D., Zhang, J., Sun, X. D., Guo, Y., Wang, Y. M., et al. (2014). Formation of a Double-decker Magnetic Flux Rope in the Sigmoidal Solar Active Region 11520. *Astrophysical Journal.* 789, 93. doi:10.1088/0004-637X/789/2/93

Cheng, X., Zhang, J., Kliem, B., Török, T., Xing, C., Zhou, Z. J., et al. (2020). Initiation and early kinematic evolution of solar eruptions. *Astrophysical Journal.* 894, 85. doi:10.3847/1538-4357/ab886a

Cheung, M. C. M., Rempel, M., Chintzoglou, G., Chen, F., Testa, P., Martínez-Sykora, J., et al. (2019). A comprehensive three-dimensional radiative magnetohydrodynamic simulation of a solar flare. *Nature Astronomy* 3, 160–166. doi:10.1038/s41550-018-0629-3

Démoulin, P. and Aulanier, G. (2010). Criteria for flux rope eruption: Non-equilibrium versus torus instability. *Astrophysical Journal.* 718, 1388–1399. doi:10.1088/0004-637X/718/2/1388

Devi, P., Démoulin, P., Chandra, R., Joshi, R., Schmieder, B., and Joshi, B. (2021). Observations of a prominence eruption and loop contraction. *Astronomy and Astrophysics.* 647, A85. doi:10.1051/0004-6361/202040042

Fan, Y. (2020). Simulations of Prominence Eruption Preceded by Large-amplitude Longitudinal Oscillations and Draining. *Astrophysical Journal.* 898, 34. doi:10.3847/1538-4357/ab9d7f

Forbes, T. G. (1990). Numerical simulation of a catastrophe model for coronal mass ejections. *Journal of Geophysics Research.* 95, 11919–11931. doi:10.1029/JA095iA08p11919

Forbes, T. G. and Priest, E. R. (1995). Photospheric magnetic field evolution and eruptive flares. *Astrophysical Journal.* 446, 377. doi:10.1086/175797

Gopalswamy, N., Akiyama, S., Yashiro, S., and Xie, H. (2018). Coronal flux ropes and their interplanetary counterparts. *Journal of Atmospheric and Solar-Terrestrial Physics* 180, 35–45. doi:10.1016/j.jastp.2017.06.004

Guo, Y., Ding, M. D., Schmieder, B., Li, H., Török, T., and Wiegelmann, T. (2010). Driving Mechanism and Onset Condition of a Confined Eruption. *Astrophysical Journal Letters.* 725, L38–L42. doi:10.1088/2041-8205/725/1/L38

Hillier, A., Hillier, R., and Tripathi, D. (2012). Determination of prominence plasma β from the dynamics of rising plumes. *Astrophysical Journal.* 761, 106. doi:10.1088/0004-637X/761/2/106

Hu, Y. Q. and Liu, W. (2000). A 2.5-dimensional ideal magnetohydrodynamic model for coronal magnetic flux ropes. *Astrophysical Journal.* 540, 1119–1125. doi:10.1086/309381

Inoue, S., Hayashi, K., Magara, T., Choe, G. S., and Park, Y. D. (2015). Magnetohydrodynamic Simulation of the X2.2 Solar Flare on 2011 February 15. II. Dynamics Connecting the Solar Flare and the Coronal Mass Ejection. *Astrophysical Journal.* 803, 73. doi:10.1088/0004-637X/803/2/73

Isenberg, P. A. and Forbes, T. G. (2007). A three-dimensional line-tied magnetic field model for solar eruptions. *Astrophysical Journal.* 670, 1453–1466. doi:10.1086/522025

Isenberg, P. A., Forbes, T. G., and Demoulin, P. (1993). Catastrophic evolution of a force-free flux rope: A model for eruptive flares. *Astrophysical Journal.* 417, 368. doi:10.1086/173319

Jenkins, J. M., Hopwood, M., Démoulin, P., Valori, G., Aulanier, G., Long, D. M., et al. (2019). Modeling the effect of mass-draining on prominence eruptions. *Astrophysical Journal.* 873, 49. doi:10.3847/1538-4357/ab037a

Jenkins, J. M., Long, D. M., van Driel-Gesztelyi, L., and Carlyle, J. (2018). Understanding the role of mass-unloading in a filament eruption. *Solar Physics.* 293, 7. doi:10.1007/s11207-017-1224-y

Jiang, C., Feng, X., Liu, R., Yan, X., Hu, Q., Moore, R. L., et al. (2021). A fundamental mechanism of solar eruption initiation. *Nature Astronomy* 5, 1126–1138. doi:10.1038/s41550-021-01414-z

Jiang, C., Wu, S. T., Yurchyshyn, V., Wang, H., Feng, X., and Hu, Q. (2016). How did a major confined flare occur in super solar active region 12192? *Astrophysical Journal.* 828, 62. doi:10.3847/0004-637X/828/1/62

Keppens, R., Guo, Y., Makwana, K., Mei, Z., Ripperda, B., Xia, C., et al. (2019). Ideal mhd instabilities for coronal mass ejections: interacting current channels and particle acceleration. *Reviews of Modern Plasma Physics* 3, 14. doi:10.1007/s41614-019-0035-z

Kliem, B., Lin, J., Forbes, T. G., Priest, E. R., and Török, T. (2014). Catastrophe versus instability for the eruption of a toroidal solar magnetic flux rope. *Astrophysical Journal.* 789, 46. doi:10.1088/0004-637X/789/1/46

Korsós, M. B., Georgoulis, M. K., Gyenge, N., Bisoi, S. K., Yu, S., Poedts, S., et al. (2020). Solar flare prediction using magnetic field diagnostics above the photosphere. *Astrophysical Journal.* 896, 119. doi:10.3847/1538-4357/ab8fa2

Lamy, P. L., Floyd, O., Boclet, B., Wojak, J., Gilardy, H., and Barlyaeva, T. (2019). Coronal mass ejections over solar cycles 23 and 24. *Space Science Reviews.* 215, 39. doi:10.1007/s11214-019-0605-y

Leka, K. D. and Barnes, G. (2007). Photospheric magnetic field properties of flaring versus flare-quiet active regions. iv. a statistically significant sample. *Astrophysical Journal.* 656, 1173–1186. doi:10.1086/510282

Li, H., Liu, Y., Elmhamdi, A., and Kordi, A.-S. (2016a). Relationship between Distribution of Magnetic Decay Index and Filament Eruptions. *Astrophysical Journal.* 830, 132. doi:10.3847/0004-637X/830/2/132

Li, T., Yang, K., Hou, Y., and Zhang, J. (2016b). Slipping Magnetic Reconnection of Flux-rope Structures as a Precursor to an Eruptive X-class Solar Flare. *Astrophysical Journal.* 830, 152. doi:10.3847/0004-637X/830/2/152

Lin, J. and Forbes, T. G. (2000). Effects of reconnection on the coronal mass ejection process. *Journal of Geophysics Research.* 105, 2375–2392. doi:10.1029/1999JA900477

Lin, J., Soon, W., and Baliunas, S. L. (2003). Theories of solar eruptions: a review. *New Astronomy Review.* 47, 53–84. doi:10.1016/S1387-6473(02)00271-3

Lin, J. and van Ballegooijen, A. A. (2002). Catastrophic and noncatastrophic mechanisms for coronal mass ejections. *Astrophysical Journal.* 576, 485–492. doi:10.1086/341737

Liu, R. (2020). Magnetic flux ropes in the solar corona: structure and evolution toward eruption. *Research in Astronomy and Astrophysics* 20, 165. doi:10.1088/1674-4527/20/10/165

Longcope, D. W. and Forbes, T. G. (2014). Breakout and tether-cutting eruption models are both catastrophic (sometimes). *Solar Physics.* 289, 2091–2122. doi:10.1007/s11207-013-0464-8

Lugaz, N., Farrugia, C. J., Winslow, R. M., Small, C. R., Manion, T., and Savani, N. P. (2017). Importance of cme radial expansion on the ability of slow cmes to drive shocks. *Astrophysical Journal.* 848, 75. doi:10.3847/1538-4357/aa8ef9

Moore, R. L., Sterling, A. C., Hudson, H. S., and Lemen, J. R. (2001). Onset of the magnetic explosion in solar flares and coronal mass ejections. *Astrophysical Journal.* 552, 833–848. doi:10.1086/320559

Priest, E. (2014). *Magnetohydrodynamics of the Sun* (Cambridge University Press)

Priest, E. R. and Forbes, T. G. (1990). Magnetic field evolution during prominence eruptions and two-ribbon flares. *Solar Physics.* 126, 319–350. doi:10.1007/BF00153054

Savcheva, A. S., van Ballegooijen, A. A., and DeLuca, E. E. (2012). Field topology analysis of a long-lasting coronal sigmoid. *Astrophysical Journal.* 744, 78. doi:10.1088/0004-637X/744/1/78

Shen, F., Shen, C., Zhang, J., Hess, P., Wang, Y., Feng, X., et al. (2014). Evolution of the 12 July 2012 CME from the Sun to the Earth: Data-constrained three-dimensional MHD simulations. *Journal of Geophysical Research (Space Physics)* 119, 7128–7141. doi:10.1002/2014JA020365

Sterling, A. C. and Moore, R. L. (2004). Evidence for Gradual External Reconnection before Explosive Eruption of a Solar Filament. *Astrophysical Journal.* 602, 1024–1036. doi:10.1086/379763

Su, Y., Surges, V., van Ballegooijen, A., DeLuca, E., and Golub, L. (2011). Observations and magnetic field modeling of the flare/coronal mass ejection event on 2010 april 8. *Astrophysical Journal.* 734, 53. doi:10.1088/0004-637X/734/1/53

Su, Y., van Ballegooijen, A., Lites, B. W., Deluca, E. E., Golub, L., Grigis, P. C., et al. (2009). Observations and Nonlinear Force-Free Field Modeling of Active Region 10953. *Astrophysical Journal.* 691, 105–114. doi:10.1088/0004-637X/691/1/105

Sun, S. J., Hu, Y. Q., and Chen, Y. (2007). Influence of photospheric magnetic flux distribution on coronal flux rope catastrophe. *Astrophysical Journal Letters.* 654, L167–L170. doi:10.1086/511304

Toriumi, S. and Wang, H. (2019). Flare-productive active regions. *Living Reviews in Solar Physics* 16, 3. doi:10.1007/s41116-019-0019-7

Török, T. and Kliem, B. (2003). The evolution of twisting coronal magnetic flux tubes. *Astronomy and Astrophysics.* 406, 1043–1059. doi:10.1051/0004-6361:20030692

Török, T., Temmer, M., Valori, G., Veronig, A. M., van Driel-Gesztelyi, L., and Vršnak, B. (2013). Initiation of coronal mass ejections by sunspot rotation. *Solar Physics.* 286, 453–477. doi:10.1007/s11207-013-0269-9

Švestka, Z. (2001). Varieties of coronal mass ejections and their relation to flares. *Space Science Reviews.* 95, 135–146. doi:10.1023/A:1005225208925

Van Tend, W. and Kuperus, M. (1978). The development of coronal electric current systems in active regions and their relation to filaments and flares. *Solar Physics.* 59, 115–127. doi:10.1007/BF00154935

Vršnak, B., Sudar, D., and Ruždjak, D. (2005). The cme-flare relationship: Are there really two types of cmes? *Astronomy and Astrophysics*. 435, 1149–1157. doi:10.1051/0004-6361:20042166

Wang, T., Sui, L., and Qiu, J. (2007). Direct observation of high-speed plasma outflows produced by magnetic reconnection in solar impulsive events. *Astrophysical Journal Letters*. 661, L207–L210. doi:10.1086/519004

Xia, C., Chen, P. F., and Keppens, R. (2012). Simulations of prominence formation in the magnetized solar corona by chromospheric heating. *Astrophysical Journal Letters*. 748, L26. doi:10.1088/2041-8205/748/2/L26

Xue, Z., Yan, X., Cheng, X., Yang, L., Su, Y., Kliem, B., et al. (2016). Observing the release of twist by magnetic reconnection in a solar filament eruption. *Nature Communications* 7, 11837. doi:10.1038/ncomms11837

Yan, X., Xue, Z., Jiang, C., Priest, E. R., Kliem, B., Yang, L., et al. (2022). Fast plasmoid-mediated reconnection in a solar flare. *Nature Communications* 13, 640. doi:10.1038/s41467-022-28269-w

Zhang, J., Dere, K. P., Howard, R. A., Kundu, M. R., and White, S. M. (2001). On the Temporal Relationship between Coronal Mass Ejections and Flares. *Astrophysical Journal*. 559, 452–462. doi:10.1086/322405

Zhang, Q., Liu, R., Wang, Y., Li, X., and Lyu, S. (2021). Confined and eruptive catastrophes of solar magnetic flux ropes caused by mass loading and unloading. *Astrophysical Journal*. 921, 172. doi:10.3847/1538-4357/ac1fef

Zhang, Q., Wang, Y., Hu, Y., Liu, R., and Liu, J. (2017a). Influence of photospheric magnetic conditions on the catastrophic behaviors of flux ropes in solar active regions. *Astrophysical Journal*. 835, 211. doi:10.3847/1538-4357/835/2/211

Zhang, Q., Wang, Y., Hu, Y., Liu, R., Liu, K., and Liu, J. (2017b). Upward and Downward Catastrophes of Coronal Magnetic Flux Ropes in Quadrupolar Magnetic Fields. *Astrophysical Journal*. 851, 96. doi:10.3847/1538-4357/aa9ce6

Zhang, Q., Wang, Y., Liu, R., Zhang, J., Hu, Y., Wang, W., et al. (2020). Eruption of solar magnetic flux ropes caused by flux feeding. *Astrophysical Journal Letters*. 898, L12. doi:10.3847/2041-8213/aba1f3